Distinct complexes containing the cytosolic type III secretion system ATPase resolved by 3D single-molecule tracking in live *Yersinia enterocolitica*

Joshua R Prindle[a], Julian Rocha[a], Yibo Wang[a], Andreas Diepold[b], Andreas Gahlmann[a,c,#]

[a]Department of Chemistry, University of Virginia, Charlottesville, Virginia, USA
[b]Max Planck Institute for Terrestrial Microbiology, Marburg, Germany
[c]Department of Molecular Physiology & Biological Physics, University of Virginia School of Medicine, Charlottesville, Virginia, USA

#Address correspondence to Andreas Gahlmann, agahlmann@virginia.edu

Abstract

The membrane-embedded injectisome, the structural component of the virulence-associated type III secretion system (T3SS), is used by gram-negative bacterial pathogens to inject species-specific effector proteins into eukaryotic host cells. The cytosolic injectisome proteins are required for export of effectors and display both stationary, injectisome-bound populations as well as freely-diffusing cytosolic populations. How the cytosolic injectisome proteins interact with each other in the cytosol and associate with membrane-embedded injectisomes remains unclear. Here, we utilize 3D single-molecule tracking to resolve distinct cytosolic complexes of injectisome proteins in living *Yersinia enterocolitica* cells. Tracking of the eYFP-labeled ATPase, *Ye*SctN, and its regulator, *Ye*SctL, reveals that these proteins form a cytosolic complex with each other and then further with *Ye*SctQ. *Ye*SctNL and *Ye*SctNLQ complexes can be observed in both in wild type cells and in Δ*sctD* mutants, which cannot assemble injectisomes. In Δ*sctQ* mutants, the relative abundance of the *Ye*SctNL complex is considerably increased. These data indicate that distinct cytosolic complexes of injectisome proteins can form prior to injectisome binding – a feature that could contribute to injectisome functional regulation.

INTRODUCTION

Bacterial type III secretion systems (T3SS) are used by gram-negative bacteria to assemble flagellar motors for cell motility and injectisomes that translocate virulence factors, called effector proteins, into eukaryotic host cells. Injectisomes are expressed by many bacterial pathogens, including *E. coli, Salmonella, Pseudomonas, Shigella,* and *Yersinia,* which are responsible for widespread human disease both historically and currently[1]. Flagellar motors and injectisomes are large, multicomponent protein structures that span two and sometimes three cell membranes, as well as the bacterial cell wall[2]. Assembly of the injectisome is achieved through hierarchal secretion of early, intermediate, and late secretion substrates[2–8]. Early secretion substrates form an extracellular needle that extends away from the bacterial cell envelope. Upon contact with a host cell, middle secretion substrates are secreted through the needle to form a translocon pore in the eukaryotic cell membrane[2–5]. Late secretion substrates, also called effector proteins, are then translocated into the host cell cytosol[6–8]. While there are species-specific differences among the effector proteins, the structural proteins of injectisomes are highly conserved[9].

Molecular-resolution structures of the fully-assembled cytosolic injectisome complex remain elusive. The cytosolic injectisome proteins SctN, L, Q, and K, associate with the injectisome loosely and transiently, so that structural imaging of fully-assembled injectisomes is only possible *in situ* through the use of cryo-electron tomography (cryo-ET)[10–14]. Injectisomes in *Salmonella* and *Shigella* minicell mutants were found to not exhibit continuous densities representative of a cytosolic ring (C-ring)[10,11], a feature that has been observed consistently for bacterial flagellar motors[4,15]. Instead, the sub-tomogram averages suggested six distinct pods composed of SctK, Q, and L that seem to cradle the hexameric ATPase[10,11]. More recently, cryo-focused ion beam milling followed by cryo-ET enabled the visualization of *Y. enterocolitica* injectisomes inside the phagosomes of infected human myeloid cells[16]. In contrast to the six distinct cytosolic pods observed in *Shigella* and *Salmonella* minicell mutants, the *Y. enterocolitica* injectisome contained more continuous, ring-like densities likely composed of SctD, K, and Q, and a 6-fold symmetric, cradle-like structure likely composed of SctL.

The cytosolic injectisome proteins have substantial freely-diffusing populations. *In vivo* fluorescence recovery after photobleaching (FRAP) experiments revealed a continual exchange (on a 1-minute time scale) between freely-diffusing and injectisome-bound states for *Ye*SctQ (*Ye* prefix indicates *Yersinia*). Interestingly, the *Ye*SctQ exchange rate at the injectisome increased by a factor of two upon chemical activation of secretion[17], suggesting that structural dynamism may be important for functional regulation of type 3 secretion. Fluorescence correlation spectroscopy (FCS) further revealed the presence of freely-diffusing and injectisome-bound populations for *Ye*SctK, L, and N[18]. In that study, the *average* diffusion rate for each cytosolic injectisome protein shifted upon chemical activation of secretion. These results further point to a dynamic and adaptive network of cytosolic interactions that may be required for injectisome binding. Earlier work from our lab identified two distinct SctQ-containing cytosolic protein complexes in living cells[19]. However, the full compositions and relative abundances of these and additional SctQ-independent cytosolic complexes are yet to be determined.

Efforts at reconstituting cytosolic injectisome protein complexes *in vitro* have begun to elucidate how these proteins may interact with one another. Native mass spectrometry (MS) experiments showed the ability of *Se*SctQ (*Se* prefix indicates *Salmonella*) to bind *Se*SctL and N with various stoichiometries. Importantly however, a *Se*SctL$_2$:*Se*SctN heterotrimer was consistently observed in any complex that included these two proteins[20]. Dynamic light scattering was used to determine the relative size of cytosolic injectisome proteins and their respective complexes[21]. Key differences were observed for reconstituted complexes containing *Sf*SctK and *Sf*SctQ and complexes containing *Sf*SctQ and *Sf*SctL (*Sf* prefix indicates *Shigella*). Specifically, the complex of *Sf*SctK and *Sf*SctQ is globular and compact (hydrodynamic diameter = 10.2 nm), whereas the complex of *Sf*SctQ and *Sf*SctL is much larger (hydrodynamic diameter = 18.5 nm). These differences were attributed to the ability of *Sf*SctQ to adopt different conformational states depending on its binding partner.

To gain further insights into how the cytosolic injectisome protein complexes interact with each other in living *Y. enterocolitica*, we use 3D single-molecule localization and tracking microscopy to resolve the different diffusive states of *Ye*SctQ, L, and N in different genetic backgrounds. Deletion of the

injectisome protein *Ye*SctD, which presumably binds *Ye*SctK[16], abrogates the clustered, membrane proximal localization of all cytosolic injectisome proteins and increases the abundance of the same cytosolic complexes that are also present in wild-type cells. We further find that deletion of *Ye*SctQ increases the abundance of a complex containing *Ye*SctN and L and eliminates the diffusive state assigned to the larger complex containing *Ye*SctN, L, and Q. These results are consistent with a model in which distinct *Ye*SctNL and *Ye*SctNLQ complexes form in the cytosol prior to binding to the injectisome.

RESULTS

*Ye*SctQ shows three prominent diffusive states in living cells

We have previously reported the diffusive behaviors of free eYFP and eYFP-labeled *Ye*SctQ in *Y. enterocolitica*[19,22]. Here, we re-analyzed these data using a more complete library of apparent diffusion coefficient distributions (see Methods). Our original conclusions remained unchanged, but the updated library enabled us to generate spectra of diffusion coefficients that manifest for labeled proteins in living bacterial cells. Transforming the raw data (cumulative distribution functions (CDFs) of apparent diffusion coefficients) into diffusion coefficient spectra addresses a key challenge in analyzing single-molecule tracking data, namely choosing a suitable fitting model among many with different numbers of parameters (diffusive states and their relative abundances)[23,24]. For freely diffusing eYFP in living *Y. enterocolitica* cells, fitting the experimental CDF of apparent diffusion coefficients using a linear combination of simulated apparent diffusion coefficient CDFs produces a diffusion coefficient spectrum exhibiting a single, well-defined peak at D = 11.5 μm^2/s (**Fig. 1a**). Non-linear fitting using a single diffusive state model, i.e. a single simulated apparent diffusion coefficient CDF, at D = 11.9 μm^2/s, results in an equally good fit (**Fig. 1b**). Thus, a single-state, confined (within the bacterial cell) Brownian diffusion model accurately describes the measured 3D motion trajectories of eYFP in living *Y. enterocolitica* cells. These results are consistent with previous work by our laboratory[22] and others[25] and confirm that eYFP has negligible (non)specific

interactions with cellular contents or with itself and is thus a suitable probe for measuring the diffusion coefficients for eYFP-labeled proteins.

In contrast to free eYFP, the diffusion coefficient spectrum of eYFP-*Ye*SctQ shows three peaks at $D \sim 1.3$, 4.8, and 15 $\mu m^2/s$ in addition to an injectisome-bound, stationary population with a peak at $D = 0$ $\mu m^2/s$ (**Fig. 1c**). eYFP-*Ye*SctQ was expressed as a genomic replacement under the control of its native promotor in actively secreting cells and the fusion protein was stable and not degraded[19]. These results are consistent with our previous fitting model[19] that identified three diffusive states for eYFP-*Ye*SctQ at $D \sim$ 1.1, 4.0, and 13.9 $\mu m^2/s$. Determining the area under the spectral peaks provides the relative population fraction of the corresponding diffusive states, while the spectral peak maxima provide an estimate of their diffusion coefficients. These parameters can then be used as a starting point for non-linear fitting of the experimental CDF of eYFP-*Ye*SctQ apparent diffusion coefficients. To test whether overfitting the data with too many different diffusive states (i.e. a non-linear model with too many free parameters) could be an issue, we initialized 1-, 2-, 3-, and 4-state fits by combining population fractions and initial guesses for diffusion coefficients from the spectrum (see Methods). Non-linear fitting of the data using a 3-state model produced diffusive states at $D \sim 1.2$, 4.4, and 14.8 $\mu m^2/s$, which agrees well with the prominent peaks in the diffusion coefficient spectrum (**Fig. 1c**). A 3-state model is also supported by 5-fold cross-validation analysis (**Supplementary Fig. 3**). We assign the fastest diffusive state of eYFP-*Ye*SctQ to the monomeric form of this protein. We note that the fitted diffusion rate of 14.8 $\mu m^2/s$ is faster than the diffusion rate of free eYFP (11.9 $\mu m^2/s$), which can be attributed to the fact that the free eYFP-expressing cells were not exposed to conditions required for secretion, i.e. a 25°→37° C temperature jump or Ca^{2+} ion chelation both factors that affect protein mobility[26].

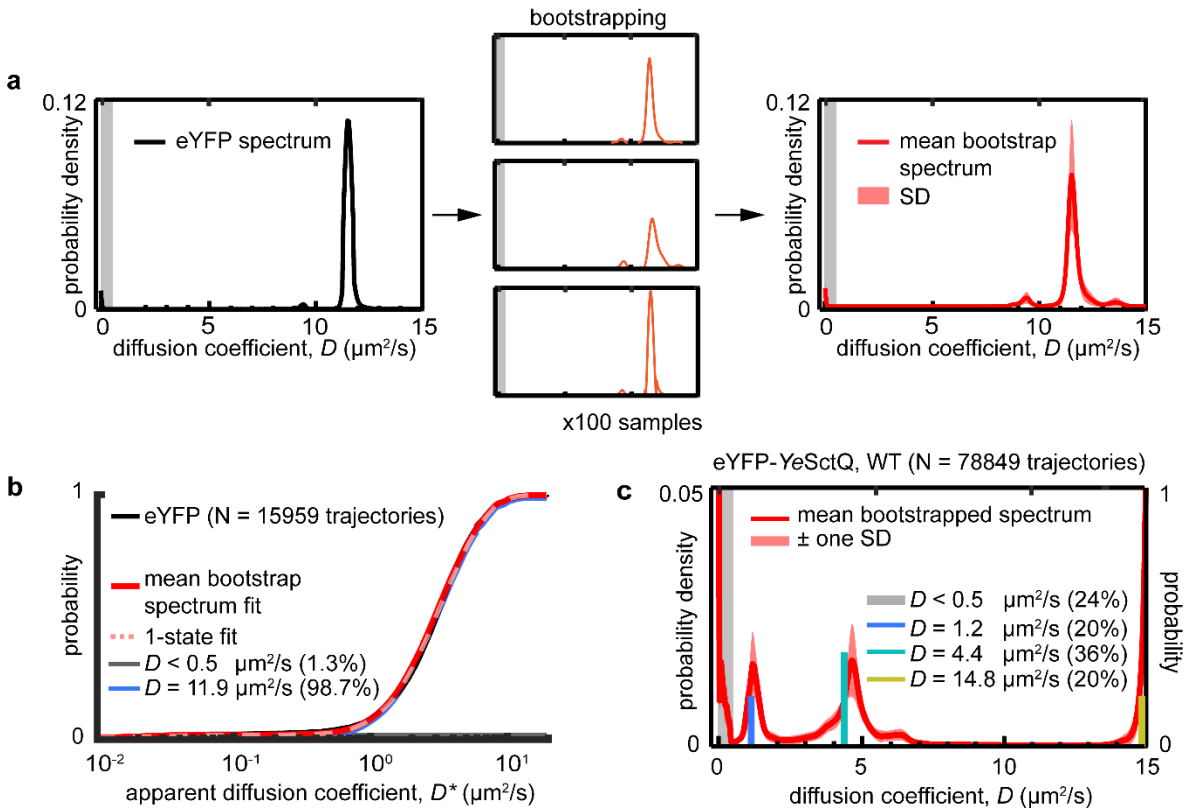

Figure 1: a) Calculation and analysis of the diffusion coefficient spectrum for freely diffusing eYFP in *Y. enterocolitica*. Previously published tracking data for free eYFP[22], expressed from the arabinose-inducible pBAD vector, produces a clear spectral peak at $D \sim 11.5$ μm^2/s. The robust presence of this peak established by bootstrapping analysis (N = 100 resampled datasets). b) Non-linear fitting result for eYFP using a 1-state model. The experimentally measured distribution is best fit with one diffusion coefficient at D = 11.9 μm^2/s, showing excellent agreement with the mean bootstrapped spectrum fit (RMSD ~ 0.36 for each). c) Diffusion coefficient analysis for eYFP-labeled *Ye*SctQ. Re-analysis of previously published tracking data for eYFP-*Ye*SctQ in wild type *Y. enterocolitica* produces three spectral peaks at $D \sim 1.3$, 4.4, and 15 μm^2/s. Non-linear fitting (see Supplementary Fig. 3) of the raw data shows that a 3-state model produces excellent agreement between the optimal fit parameters and spectrum peaks.

*Ye*SctL shares one diffusive state with *Ye*SctQ

Having reproduced our previously obtained results in the diffusion coefficient spectra, we next analyzed the intracellular diffusive behaviors of eYFP-labeled *Ye*SctL. We had previously tracked *Ye*SctL with PAmCherry1, but chose to switch the fluorescent label to eYFP for the present study due to its homogeneous diffusion behavior in *Y. enterocolitica* (**Fig. 1ab**). Again, we expressed eYFP-*Ye*SctL as a genomic replacement under the control of its native promotor. The eYFP-*Ye*SctL fusion protein was

functional and not degraded (**Supplementary Fig. 1 & 2**). Examination of the eYFP-*Ye*SctL diffusion coefficient spectrum reveals a prominent spectral peak at $D \sim 1.3$ and 15 μm^2/s and smaller peaks at $D \sim 2.8$ and 4.0 μm^2/s (**Fig. 2a**). The 4-state model for eYFP-*Ye*SctL produced diffusive states at $D \sim 0.9$ (population fraction = 10%), 2.2 (population fraction = 10%), and 4.0 μm^2/s (population fraction = 3%) as well as a faster moving state. Given that the diffusion coefficient spectrum clearly indicates a prominent peak at $D \sim 1.3$ μm^2/s and does not include a peak at $D \sim 0.9$ μm^2/s, we turned to the 3-state model, whose fitted values agree better with the spectral peak positions. The choice of the 3-state model is also supported by 5-fold cross-validation analysis (**Supplementary Fig. 4**).

The 3-state model provides three diffusive states for eYFP-*Ye*SctL at $D \sim 1.1$, 2.9, and 15 μm^2/s and corresponding population fractions of 12%, 11%, and 6%, respectively (**Fig. 2a, Supplementary Fig. 4**). These mobile states are in addition to an abundant (population fraction = 71%) stationary, injectisome-bound population with $D < 0.5$ μm^2/s. Plotting the 3D trajectories using a $D^* = 0.5$ μm^2/s threshold clearly shows membrane-associated clusters representing the injectisome-bound population (**Fig. 2b**). We assign the diffusive state at $D \sim 15$ μm^2/s to freely-diffusing monomeric eYFP-*Ye*SctL based on the same arguments made above for eYFP-*Ye*SctQ. The $D \sim 1.1$ μm^2/s diffusive state is consistent with our previous result obtained with PAmCherry-*Ye*SctL, based on which we concluded that both eYFP-*Ye*SctQ and eYFP-*Ye*SctL diffuse at the same slow rate as part of the same complex[19]. The SctLQ interaction is also supported by a number of previous studies[18,20,21]. On the other hand, the $D \sim 2.9$ μm^2/s eYFP-*Ye*SctL diffusive state has not been previously observed. The presence of this additional state suggests another homo- or hetero-oligomeric complex containing *Ye*SctL. However, such a complex does not contain *Ye*SctQ, because a $D \sim 2.9$ μm^2/s diffusive state is not observed in the eYFP-*Ye*SctQ data.

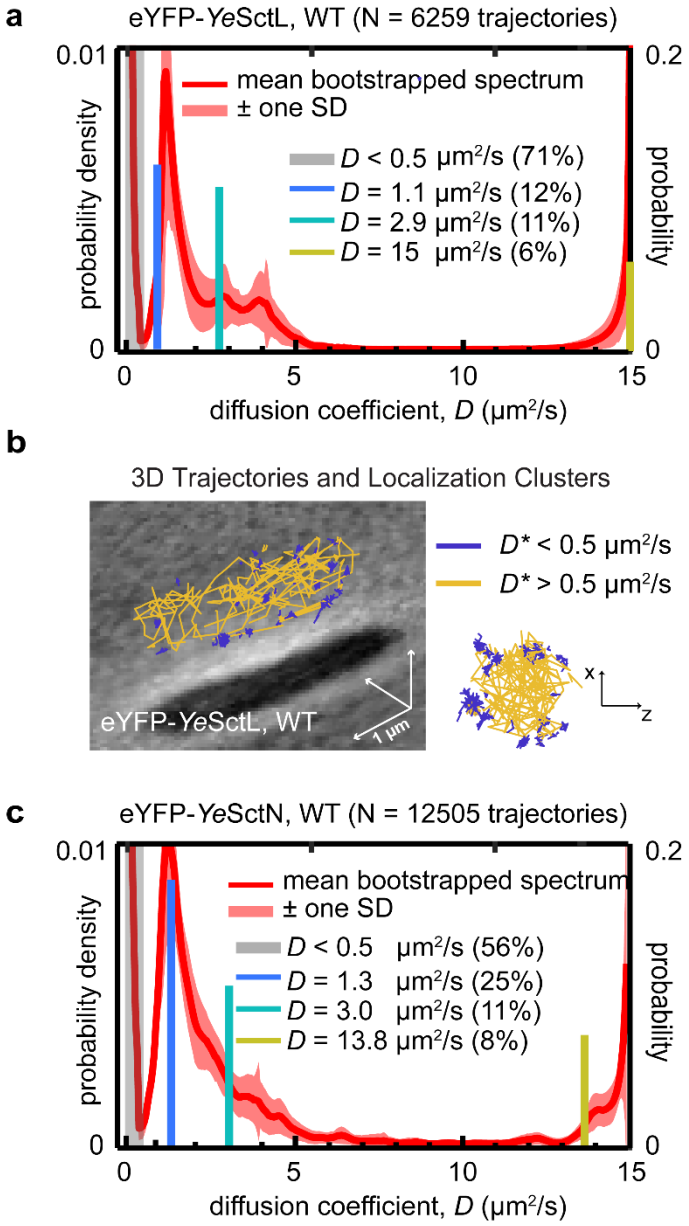

Figure 2: a) Diffusion coefficient spectrum for eYFP-*Ye*SctL and in wild type cells. The experimentally measured distribution is best fit with two states at $D = 1.1$ μm²/s and $D \sim 2.9$ μm²/s as well as a fast-diffusing state (Supplementary Figure 4). b) 3D trajectories for eYFP-*Ye*SctL with $D^* < 0.5$ μm²/s exhibit clustering at the membrane indicative of association with injectisomes. c) Diffusion coefficient spectrum for eYFP-*Ye*SctN and in wild type cells. The experimentally measured distribution is best fit with three diffusive states at $D = 1.3$ μm²/s, $D \sim 3.0$ μm²/s, and $D \sim 13.8$ μm²/s (Supplementary Figure 5).

*Ye*SctN and *Ye*SctL share two distinct diffusive states in *Y. enterocolitica*

There are numerous reports documenting interactions between SctN and SctL in both flagellar and virulence-associated T3SSs[27–30]. SctL binding prevents SctN hexamerization prior to injectisome binding and thereby negatively regulates SctN's ATPase activity, which is the one of the most well-established functional roles of the cytosolic injectisome proteins[27,29,31–34]. To detect the SctNL interaction in living cells, we expressed eYFP-*Ye*SctN as a genomic replacement under the control of its native promotor and acquired eYFP-*Ye*SctN single-molecule trajectories in actively secreting cells. The eYFP-*Ye*SctN fusion protein was functional and only minimally degraded (**Supplementary Fig. 1 & 2**). The resulting diffusion coefficient spectrum shows very prominent spectral peaks at $D \sim 1.3$ and 15 $\mu m^2/s$ (**Fig. 2c**). However, non-linear fitting with a 2-state model produces diffusive states at $D \sim 1.2$ and 6 $\mu m^2/s$, a result that does not agree with the diffusion coefficient spectrum. In contrast, a 3-state models produces diffusive states at $D \sim 1.3$, 3.0, and 13.8 $\mu m^2/s$ with corresponding population fractions of 25%, 11%, and 8% (**Fig. 2c**, **Supplementary Fig. 5**), a result that better matches the diffusion coefficient spectrum. The 3-state model is also supported by cross-validation analysis (**Supplementary Fig. 5**). Again, we assign the fast-diffusive state to the eYFP-*Ye*SctN monomer. The robust emergence of a $D \sim 1.3$ $\mu m^2/s$ diffusive state, a state that is also observed in YeSctL and YeSctQ measurements, in both the 2- and 3-state models suggests the formation of a hetero-oligomeric *Ye*SctNLQ complex. The 3-state model produces an intermediate diffusive state at $D \sim 3.0$ $\mu m^2/s$ and such a diffusive state was also observed for eYFP-*Ye*SctL ($D \sim 2.9$ $\mu m^2/s$). We thus tentatively assign this diffusive state to SctNL complex. While the SctNL interaction is supported by a number of previous studies, the population fractions of this state is low (<11%) for both eYFP-*Ye*SctN and eYFP-*Ye*SctL in wild-type cells. We therefore concluded that establishing the existence of this state needed further experimental support.

We argued above that the oligomeric complex that gives rise to the $D \sim 3.0$ $\mu m^2/s$ diffusive state does not contain *Ye*SctQ. It follows that deletion of *sctQ* should not affect the formation of that complex. To test this hypothesis, we acquired single-molecule trajectories for eYFP-*Ye*SctN and eYFP-*Ye*SctL in a Δ*sctQ* mutant background. Remarkably, the CDFs of apparent diffusion coefficients for these two proteins

(i.e. the raw data) are essentially congruent in the Δ*sctQ* background, strongly indicating co-diffusive behavior (**Fig. 3a**). Plotting the 3D trajectories for eYFP-*Ye*SctN in the Δ*sctQ* background using a $D^* = 0.5$ $\mu m^2/s$ threshold shows an absence of membrane-associated clusters (**Fig. 3b**). The same phenomenon is observed for eYFP-*Ye*SctL in the Δ*sctQ* background (data not shown), indicating that injectisome association is no longer possible in the absence of SctQ[18]. The spectra of diffusion coefficients of these two proteins show the same trend: each spectrum contains two prominent peaks at $D \sim 2.8$ and 15 $\mu m^2/s$. Notably, a peak at $D \sim 1.3$ $\mu m^2/s$, which we previously assigned to a *Ye*SctNLQ complex, is also absent. A 2-state non-linear fit converged on $D \sim 2.6$ and 15 $\mu m^2/s$ in each case with corresponding population fractions of 83% and 8% for eYFP-*Ye*SctL and 85% and 7% for eYFP-*Ye*SctN, respectively (**Supplementary Fig. 6, Supplementary Fig. 7**).

Together, these results support the conclusion that *Ye*SctL and *Ye*SctN are able to form two distinct cytosolic complexes. One of these complexes contains *Ye*SctQ and the other does not. Under our experimental conditions, the *Ye*SctNLQ complex diffuses at $D \sim 1.3$ $\mu m^2/s$, while the *Ye*SctNL complex diffuses at $D \sim 2.8$ $\mu m^2/s$. In wild-type cells, the presence of *Ye*SctQ leads to a smaller abundance of the *Ye*SctNL complex in favor of the *Ye*SctNLQ complex as well as injectisome-bound *Ye*SctL and *Ye*SctN.

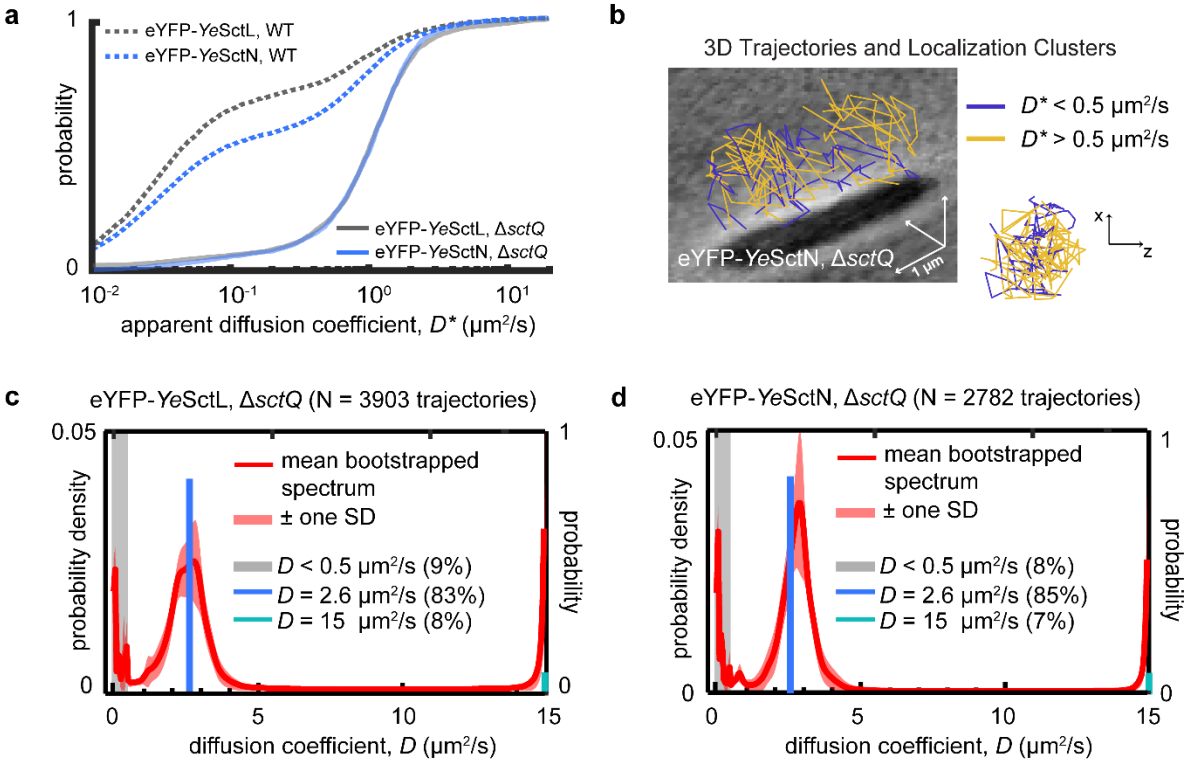

Figure 3: a) Experimentally measured CDFs eYFP-*Ye*SctL and eYFP-*Ye*SctN apparent diffusion coefficients in wild type cells and Δ*sctQ* mutants. The distributions overlay very well upon removal of *Ye*SctQ. b) 3D trajectories for eYFP-*Ye*SctN in the Δ*sctQ* background show an absence of membrane-associated clusters for $D^* < 0.5$ μm²/s. c) and d) Diffusion coefficient spectra for eYFP-*Ye*SctL and eYFP-*Ye*SctN and in the Δ*sctQ* background. In each case, the experimentally measured distribution is best fit with two states at $D = 2.6$ μm²/s and $D \sim 15$ μm²/s (Supplementary Figure 6 & 7).

Native complex formation among *Ye*SctQ, L, and N increases in the absence of injectisomes

SctD is the inner-membrane ring protein of the injectisome. SctD is required for proper injectisome assembly[35] and subsequent effector protein secretion. SctD provides a binding interface for SctK, which in turn allows SctQ, L, and N to bind to the injectisome[36]. Thus, SctQ, L, and N are completely cytosolic in the Δ*sctD* background. To test whether the same diffusive states manifest in the absence of fully-assembled injectisomes, we acquired single-molecule trajectories in the Δ*sctD* mutant background for eYFP-*Ye*SctQ, eYFP-*Ye*SctL, and eYFP-*Ye*SctN.

The Δ*sctD* eYFP-*Ye*SctQ spectrum is very similar to the spectrum observed in wild-type eYFP-*Ye*SctQ cells. Three clear spectral peaks are evident at $D \sim 1.3$, 4.8, and 15 μm²/s (**Fig. 4a, Supplementary**

Fig. 8). A 3-state non-linear fit produces diffusive states at D ~ 1.2, 4.4 and 14.9 μm^2/s, a result that is in excellent agreement with the diffusive state observed in wild-type cells. These data show that the same complexes formed in wild-type cells can also form in the absence of injectisomes. Consistent with the loss of injectisome binding, the combined population fractions of the three distinct cytosolic diffusive states increase. The D < 0.5 μm^2/s state(s) decreased from 24% in wild-type cells to 8% in the Δ*sctD* mutant. We note however that the 8% of slow diffusing molecules in the Δ*sctD* mutant do not localize to the membrane (**Supplementary Fig. 11**).

The eYFP-*Ye*SctL and eYFP-*Ye*SctN Δ*sctD* spectra both show a broad peak extending from D ~ 1 to 4 μm^2/s. A 3-state fit converges to diffusive states at D ~ 1.2, 2.4, and 13 μm^2/s for eYFP-*Ye*SctL and D ~ 1.2, 2.5, and 15 μm^2/s for eYFP-*Ye*SctN. Both of these results agree well with the diffusion coefficient spectra (**Fig. 4bc, Supplementary Fig. 9, Supplementary Fig. 10)** and are in also in close agreement with the diffusive states observed for each protein in wild-type and Δ*sctQ* cells. Taken together, these results establish that the same complexes formed in wild-type cells can also form, in increased abundance, in the absence of injectisomes.

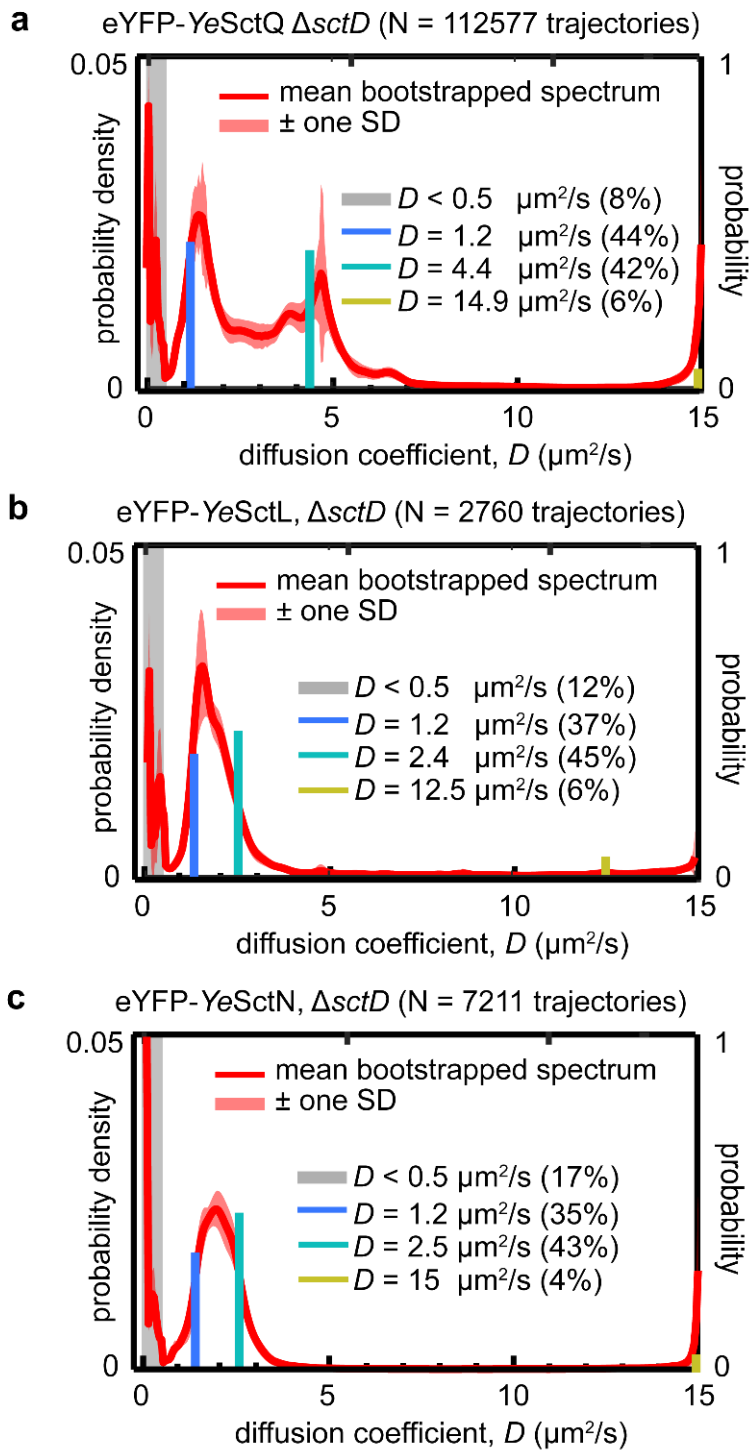

Figure 4: Removal of *Ye*SctD results in an increased abundance of native cytosolic complexes. a) eYFP-*Ye*SctQ, b) eYFP-*Ye*SctL, and c) eYFP-*Ye*SctN all share a diffusive state at $D \sim 1.3$ μm^2/s, consistent with results obtained in wild type cells. Also consistent with wild type results is the presence of a diffusive state at $D \sim 4.4$ μm^2/s for *Ye*SctQ and the presence of a shared diffusive state for *Ye*SctL and *Ye*SctN at $D \sim 2.5$ μm^2/s.

DISCUSSION

Determining the functional role(s) of the cytosolic injectisome proteins has been challenging, because our understanding of their interactions at the injectisome and in the cytosol remains limited. Here, we present live-cell single-molecule tracking data that suggest the formation of distinct, freely-diffusing protein complexes. One complex containing *Ye*SctN and *Ye*SctL, but not *Ye*SctQ, diffuses at $D \sim 2.8$ μm^2/s. A larger complex containing *Ye*SctN, L, and Q diffuses at $D \sim 1.3$ μm^2/s. These complexes form robustly in wild-type and mutant cells that are unable to fully assemble T3SS injectisomes (**Fig. 5**).

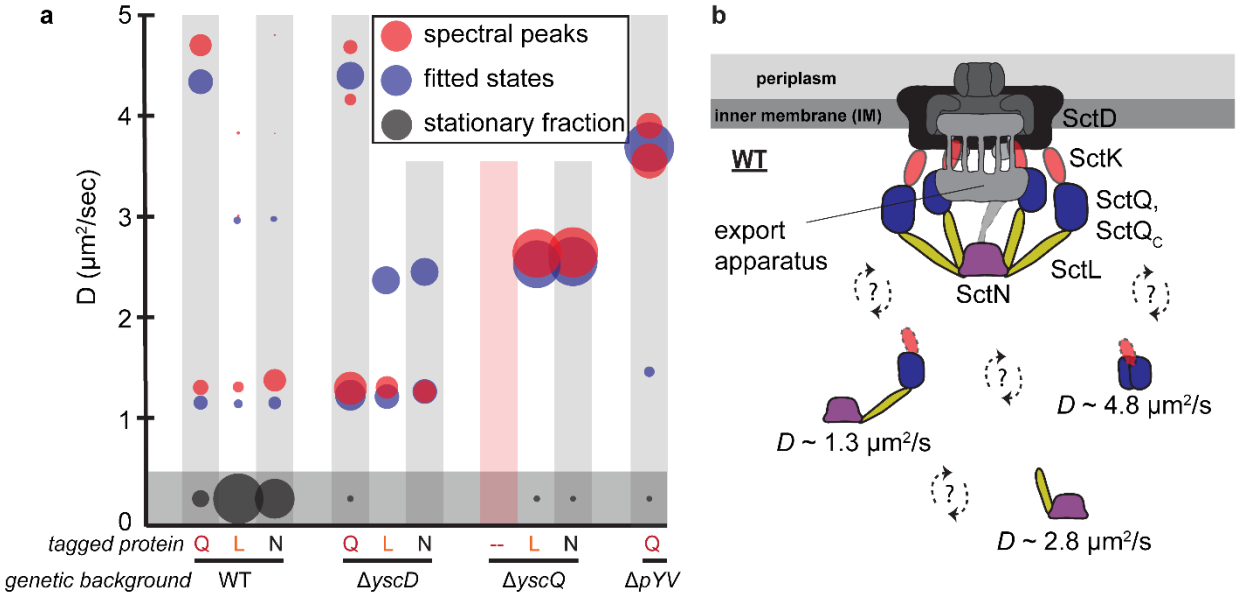

Figure 5: a) Comparison of spectral peaks and fitted diffusive states for each eYFP-labeled protein tracked in different genetic backgrounds. The relative population fraction for each peak/diffusive state is represented by the size of the circle. Spectra for eYFP-*Ye*SctN and eYFP-*Ye*SctL in the Δ*sctD* mutant do not contain prominent spectral peaks corresponding to the fitted $D \sim 2.8$ μm^2/s diffusive state, whereas prominent spectral peaks are resolved in the Δ*sctQ* mutant. The fitted diffusive states for $D < 0.5$ μm^2/s in the Δ*sctD*, Δ*sctQ*, and Δ*pYV* mutants do not localize to the membrane. b) Proposed model for cytosolic injectisome protein complex formation in living *Yersinia enterocolitica*. These complexes form in the presence and in the absence of injectisomes, supporting the formation of distinct cytosolic injectisome protein complexes prior to association with injectisomes. These complexes may exchange with each other or with injectisomes, as shown by the hypothesized exchange arrows.

A *Ye*SctNL complex is consistent with a proposed regulatory mechanism of *Ye*SctL. SctL is thought to negatively regulate ATPase activity in both bacterial flagellar motors and injectisomes by preventing

SctN hexamerization in the cytosol[29]. Recent cryo-EM data on purified proteins show that the extreme N-terminus of FliI (the flagellar homologue of SctN) contains a charged region to which FliH (the flagellar homologue of SctL) can bind[37]. Abolishing this interaction through point mutations results in a higher propensity of ATPase hexamerization *in vitro*, as well as decreased cell growth and cell motility phenotypes. Further, the SctNL (FliIH) complex has been consistently observed as a heterotrimer using *in vitro* biochemical and biophysical approaches[12,20,27,32,33,38,39], with a dimer of SctL (FliH) binding to the ATPase monomer SctN (FliI). Based on these results, we posit that the $D \sim 2.8$ μm^2/s diffusive state that we observe both wild-type and Δ*sctQ* mutants and the $D \sim 2.5$ μm^2/s diffusive state that we observe in Δ*sctD* mutants is likely due to a *Ye*SctN$_1$:*Ye*SctL$_2$ heterotrimer. In wild-type cells, 11% of *Ye*SctN and 12% of *Ye*SctL contribute to this heterotrimer population. In Δ*sctQ* and Δ*sctD* mutants, the abundance of this heterotrimer increases dramatically (85% and 83% for *Ye*SctN and *Ye*SctL, respectively, for Δ*sctQ* and 43% and 45% for *Ye*SctN and *Ye*SctL, respectively, for Δ*sctD*).

A *Ye*SctNLQ complex is consistent with cytosolic pod complexes containing SctN, L, Q, and K. Sub-tomogram averages in *Shigella* and *Salmonella* suggest six distinct pods composed of SctK, Q, and L that seem to cradle the hexameric ATPase at the injectisome[10,11]. Subsequent work has focused on reconstituting such pod complexes *in vitro*. *Se*SctNLQ[20] and *Sf*SctLQK complexes[21] were successfully isolated, and the estimated size and shapes of these complexes were qualitatively consistent with cryo-ET pod densities. Based on these results, we speculate that the $D \sim 1.3$ μm^2/s diffusive state we observe in wild-type cells and in Δ*sctD* mutants is likely not just a SctNLQ complex, but a SctNLQK heterooligomer. This claim is substantiated by the loss of the $D \sim 1.3$ μm^2/s diffusive state when we track eYFP-*Ye*SctL and eYFP-*Ye*SctN proteins in the Δ*sctQ* mutant. Whether a $D \sim 1.3$ μm^2/s diffusive state also manifests for SctK, however, remains to be determined.

The molecular composition of the $D \sim 4.8$ μm^2/s diffusive state observed for eYFP-*Ye*SctQ could be consistent with a *Ye*SctQK complex. In our previous work[19], we assigned this intermediate diffusive state to a *Ye*SctQ homo-oligomer that also contains *Ye*SctQ$_C$, the alternatively expressed C-terminal fragment of *Ye*SctQ. This assignment was made based on tracking eYFP-*Ye*SctQ proteins in a Δ*pYV* mutant,

which does not express any other T3SS proteins. In that mutant, ~80% of the tracked proteins diffused at D ~ 3.6 μm^2/s, which is notably smaller than the D ~ 4.8 μm^2/s diffusive state that we observe in wild type cells. This discrepancy indicates that the corresponding diffusive states likely originate from different complexes. The spectrum of eYFP-*Ye*SctQ diffusion coefficients in a Δ*pYV* background indeed show a prominent spectral peak ranging from D ~ 3 to 4.5 μm^2/s, but little spectral density at D ~ 4.8 μm^2/s (**Supplementary Fig. 12**). *In vitro* light-scattering measurements on *Sf*SctQ-containing complexes by Tachiyama *et al.*[21] suggested the ability of *Sf*SctQ to adopt different conformational states depending on its interacting partner. A small, globular complex (hydrodynamic diameter = 10.2 nm) was observed upon co-expression and co-purification of *Sf*SctQ and K, while a larger complex (hydrodynamic diameter = 13.4 nm) was observed for co-purified *Sf*SctQ and Q_C. Based on these results, we speculate that the D ~ 4.8 μm^2/s diffusive state in wild type cells and in Δ*sctD* mutants is in fact due to a *Ye*SctQK complex. In wild-type cells, we observe very little spectral density in the D = 3.5 - 4 μm^2/s range, which indicates that a *Ye*SctQQ_C complex is not abundantly present. On the other hand, if injectisomes are not assembled, as in the Δ*sctD* mutants, we do observe spectral density in the D = 3.5 - 4 μm^2/s range. These results indicate that the presence of injectisomes and thus the ability of *Ye*SctQ to bind to and unbind from injectisomes affects the type of complexes that *Ye*SctQ forms in abundance. Determining the compositions and stoichiometries of *Ye*SctQ-containing complexes in specific deletion mutants will be the subject of future work.

Complex formation among cytosolic injectisome proteins may provide the foundation for functional regulation of type 3 secretion. Specifically, a pool of freely diffusing complexes of injectisome proteins that are available for injectisomes binding would provide a mechanism for timely reactivation of secretion. Recent work has shown that an extracellular pH drop from 7 to 4 results in disassociation of *Ye*SctN, L, Q, and K from injectisomes, an effect that correlated with loss of secretion[40]. Notably, the intracellular pH decreased only slightly (pH=7→6.3) in acidic extracellular environments. Reverting the external pH from 4 to 7 reverses these effects. Injectisome binding is restored within ~10 min and effector protein secretion resumes shortly thereafter. The results reported here lend further support for a secretion

reactivation model relying on cytosolic complexes of injectisome proteins: in Δ*sctQ* and in Δ*sctD* mutants, in which injectisome binding is not possible, we observe clear signatures of the same diffusive states in wild-type cells that we assign to distinct *Ye*SctNLQ, *Ye*SctNL, and *Ye*SctQK complexes.

Identifying which cytosolic injectisome proteins assemble into freely-diffusing complexes in a native biological context can help determine how these proteins bind and unbind dynamically to and from injectisomes. While we have identified the compositions of three prominent complexes, the stoichiometries and functions of these complexes remains to be determined. Earlier studies suggested that SctK, Q, Q_C, L, and possibly N, form a high molecular weight (>1MDa) complex, termed the sorting platform, that sequentially interacts with different secretion substrates and their chaperones[41,42]. However, efforts aimed at reconstituting sorting platform complexes *in vitro* have not been reported. There is also no direct evidence of chaperone-effector complex binding to the injectisome-bound sorting platform or ATPase in intact cells. In the context of fully functioning T3SSs, these interactions may be transient, as whole-cell microscopy experiments only show a disperse distribution of secretion substrates in the cytosol[43]. However, the flagellar homologue of the $SctN_1$:$SctL_2$ heterotrimer has been shown to bind secretion substrates and was thus proposed to shuttle them to the flagellar T3SS[32,33,44–46]. Previous work has also shown that average diffusion rate of the cytosolic injectisome proteins shifts upon chemical-induction of secretion[18]. Future work will need to determine the molecular structures of the complexes identified here and how their individual abundances change in response to environmental signals that induce T3SS assembly and activate secretion. Such efforts will help determine how the cytosolic injectisome proteins interact when bound to injectisomes and in the cytosol and how their dynamic exchange at injectisomes contributes to functional regulation of secretion.

MATERIALS AND METHODS

Bacterial Strains

Yersinia enterocolitica strains expressing fluorescent fusion proteins were generated by allelic exchange as previously described[35,47]. Mutator plasmids containing 250-500bp flanking regions, the coding sequence for eYFP, and a 13 amino acid flexible linker region between the fluorescent and target protein were introduced into *E. coli* SM10 λpir for conjugation with *Y. enterocolitica* pIML421asd. After sucrose counter-selection for the second allelic exchange event, colonies were grown overnight in BHI media (Sigma Aldrich, St. Louis, Missouri) with nalidixic acid (Sigma Aldrich) [35 µg/mL] and 2,6-diaminopimelic acid (Chem Impex International, Wood Dale, Illinois) [80 µg/mL]. PCR screening was then performed to confirm target insertion and constructs were confirmed by sequencing (GeneWiz, South Plainfield, New Jersey).

Cell Culture

Yersinia enterocolitica strains were inoculated from freezer stock one day prior to imaging and grown overnight in BHI media containing nalidixic acid (NaI) [35 µg/mL] and 2,6-diaminopimelic acid (dap) [80 µg/mL] at 28°C with shaking. On the day of imaging, 250 µL of overnight culture were transferred into fresh BHI media containing NaI, and dap and grown at 28°C with shaking for one hour. Glycerol [4 mg/mL], $MgCl_2$ [20 mM] and EDTA [5 mM] were then added to culture medium and transferred to a 37°C water bath with shaking for 3 hours to induce expression of the *yop* regulon and ensure secretion activation, respectively. Cells were pelleted by centrifugation at 5000x g for 3 minutes and resuspended three times into fresh M2G (4.9 mM Na_2HPO_4, 3.1 mM KH_2PO_4, 7.5 mM NH_4Cl, 0.5 mM $MgSO_4$, 10 µM $FeSO_4$ (EDTA chelate; Sigma), 0.5 mM $CaCl_2$) with 0.2% glucose as the sole carbon source. After the three washes, the remaining pellet was re-suspended in M2G, dap, $MgCl_2$, glycerol, and EDTA/$CaCl_2$. Cells were finally plated on 1.5 – 2% agarose pads in M2G containing dap, glycerol, and $MgCl_2$.

Secretion assay and protein analysis

Cultures were inoculated to an optical density at 600 nm of 0.12 from stationary overnight cultures. After 1.5 h of growth at 28°C, induction of the *yop* regulon was performed by shifting the culture to 37°C. Cultures were further incubated at 37°C for 3 hours. Bacteria from 2 ml culture were collected (15,000 g, 10 min, 4°C). 1.8 ml of supernatant was mixed with 0.2 ml trichloroacetic acid (final concentration 10%) and incubated over night at 4°C to precipitate proteins within the supernatant. Proteins were collected (15,000 g, 15 min, 4°C) and washed twice with ice-cold acetone (15,000 g, 5 min, 4°C). The pellet was dried at room temperature for 1 h. The pellet was resuspended in SDS-PAGE loading buffer (SDS (2% w/v), Tris-HCl (0.1 M), glycerol (10% w/v), DTT (0.05 M), pH = 6.8) and 0.6 OD units (1 OD unit is the equivalent of 1 ml culture at an OD_{600} of 1) in 15 µl were used for the SDS-PAGE gel analysis. For Western Blot analysis of the total cellular sample, the collected bacterial pellet was prepared for Western blot analysis by directly normalizing to 0.3 OD units in 15 µl loading buffer. All samples were heated for 10 min at 99°C before loading. Proteins were separated by SDS-PAGE on 15% acrylamide gels. For visualization, the gels were stained with InstantBlue (Expedeon). For immunoblots, the proteins were blotted on a nitrocellulose membrane. Detection of the eYFP-tag was performed by using primary rabbit antibodies against GFP (1:5000) (Invitrogen A6455, lot #1853896) and secondary anti-rabbit antibodies conjugated with horseradish peroxidase (1:10,000) (Sigma A8275). The immunoblot was visualized using ECL chemiluminescence substrate (Pierce) on a LAS-4000 Luminescence Image Analyzer (Fujifilm).

Single-Molecule Super-Resolution Fluorescence Imaging

Image data were acquired on a custom-built inverted fluorescence microscope based on the RM21 platform (Mad City Labs, Inc, Madison, Wisconsin), as previously described[19,22]. Immersion oil was placed between the objective lens (UPLSAPO 100 1.4 NA) and the glass cover slip (VWR, Radnor, Pennsylvania, #1.5, 22 mm 22 mm). Single-molecule images were obtained by utilizing eYFP photoblinking[48]. A 514 nm laser (Coherent, Santa Clara, California, Genesis MX514 MTM) was used for excitation of eYFP (B350 W cm2). Zero order quarter wave plates (Thorlabs, Newton, New Jersey, WPQ05M-405, WPQ05M-514,

WPQ05M-561) were used to circularly polarize all excitation lasers, and the spectral profile of the 514 nm laser was filtered using a bandpass filter (Chroma, Bellows Falls, Vermont, ET510/10 bp). Fluorescence emission from both eYFP was passed through a shared filter set (Semrock, Rochester, New York, LP02-514RU-25, Semrock NF03-561E-25, and Chroma ET700SP-2P8). The emission path contains a wavelength specific dielectric phase mask (Double Helix, LLC, Boulder, Colorado) that is placed in the Fourier plane of the microscope to generate a double-helix point-spread-function[49,50] (DHPSF). The fluorescence signals is detected on a sCMOS cameras (Hamamatsu, Bridgewater, New Jersey, ORCA-Flash 4.0 V2). Up to 20 000 frames are collected per field-of-view with an exposure time of 25 ms. A flip-mirror in the emission pathway enables toggling the microscope between fluorescence imaging and phase contrast imaging modes without having to change the objective lens of the microscope.

Data Processing

All fluorescence images were processed in MatLab using a modified version of the easyDHPSF code[19,22,51]. To extract 3D localizations, fluorescence intensity from single-molecule emitters was fit to a double-Gaussian PSF model with maximum likelihood estimation. A median filter with a time window of 10 frames was used for background subtraction.

For each field-of-view, cell outlines were generated based on the phase contrast images using the open-source software OUFTI[52]. Single-molecule localizations were then overlayed and aligned with the cell outlines. To ensure that single-molecule localizations align well with the corresponding cell, the cell outlines are registered to the fluorescence data by a two-step 2D affine transformation using the 'cp2tform' function in MATLAB. Five control points were manually selected based on the position of the cell poles of single-molecule localization data, which generated an initial transformation that allow for the removal of any cell containing less than 10 localizations. The center of mass for all the remining cells were then used to create a second, larger set of control pairs to compute the final transformation function. Only localizations within cell outlines were considered for further analysis.

Single-molecule Tracking Analysis

3D single-molecule localizations were linked into trajectories with a distance threshold of less than 2.5 µm between subsequent localizations. If two or more localizations were present in the cell at the same time, the trajectory was not considered for further analysis to prevent the incorporation of two or more molecules into the same trajectory. Any trajectories containing less than 4 localizations were also not considered for further analysis.

Trajectory information was then used to calculate the Mean Square Displacement (MSD)

$$MSD = \frac{1}{N}\sum_{n=2}^{N}\left(x_n - x_{n-1}\right)^2$$

where N is the total number of time points and x_n is the 3D position of the molecule at time point n. The apparent diffusion coefficient, D^*, of a given molecule trajectory was then computed as

$$D^* = \frac{MSD}{2 \cdot m \cdot \Delta t}$$

where $m=3$ is the dimensionality of the data and Δt is the camera exposure time. Δt=25 ms for all experiments reported here.

Monte Carlo Simulations

To resolve the unconfined diffusion coefficients of distinct molecular complexes in living cells based on the experimentally measured distribution of apparent diffusion coefficients, we simulated confined Brownian motion trajectories inside a cylindrical volume (radius = 0.4 μm, length = 5 μm). We added to our existing pool[22] of simulated diffusion coefficients to improve data fitting (see next section). Noisy, motion-blurred single-molecule images mimicking the raw experimental data were simulated for confined (in the cylindrical volume) single-molecules with defined Brownian diffusion coefficients. These images were then processed and linked into trajectories in the same manner as our experimental data. The resulting simulated CDFs account for confinement effects of the bacterial cell volume, signal integration over the camera exposure time, and experimentally calibrated signal-to-noise levels. Analyzing the simulation data

in the same manner as experimental data ensures that static and dynamic localization errors[22] are accurately modeled for our data fitting routine.

Data Fitting

Experimental distributions of apparent diffusion coefficients were fit using a linear combination of simulated CDFs, where each CDF corresponds to a single diffusive state described by a single diffusion coefficient. The coefficients of the best fitting linear combination were determined using the Matlab function lsqlin() with the trust-region-reflective algorithm (The MathWorks, Inc, Natick, MA). The resulting linear coefficients can be displayed as a spectrum of diffusion coefficients that manifest for a tracked protein in living cells. To establish the robustness of individual peaks in the diffusion coefficient spectrum, we resampled the raw data using bootstrapping (N = 100). We then average these bootstrapped spectra and used the resulting linear coefficients to fit the experimental data (mean bootstrapped spectrum fit). The mean bootstrapped spectrum provides us with an initial estimate of the diffusion coefficients of prominent diffusive states and their relative population fractions, estimated by determining the peak maxima and the area under the spectral peaks, respectively. The so-obtained parameters are then used as input parameters for non-linear fitting using the particleswarm() function in MATLAB. This approach allowed us to estimate the diffusion coefficients and population fractions of distinct diffusive states that manifest in living cells. In the case where the spectrum contains overlapping peaks or feature-less non-zero spectral density, we choose one or multiple diffusive states to initialize the non-linear fitting process. This approach results in the *n*-state (n = 1-4) fitting models shown in Supplementary Figs. 3-10, which are then evaluated using 5-fold cross-validation and qualitative agreement with the diffusion coefficient spectrum obtained by linear fitting.

References

1. Coburn, B., Sekirov, I. & Finlay, B. B. Type III Secretion Systems and Disease. *Clin. Microbiol. Rev.* **20**, 535–549 (2007).
2. Deng, W. *et al.* Assembly, structure, function and regulation of type III secretion systems. *Nat. Rev. Microbiol.* **15**, 323–337 (2017).
3. Diepold, A. Assembly and Post-assembly Turnover and Dynamics in the Type III Secretion System. in *Bacterial Type III Protein Secretion Systems* (eds. Wagner, S. & Galan, J. E.) 35–66 (Springer International Publishing, 2020). doi:10.1007/82_2019_164.
4. Diepold, A. & Armitage, J. P. Type III secretion systems: the bacterial flagellum and the injectisome. *Philos. Trans. R. Soc. B Biol. Sci.* **370**, 20150020 (2015).
5. Burkinshaw, B. J. & Strynadka, N. C. J. Assembly and structure of the T3SS. *Biochim. Biophys. Acta BBA - Mol. Cell Res.* **1843**, 1649–1663 (2014).
6. Wagner, S. *et al.* Bacterial type III secretion systems: a complex device for the delivery of bacterial effector proteins into eukaryotic host cells. *FEMS Microbiol. Lett.* **365**, (2018).
7. Lara-Tejero, M. & Galán, J. E. The Injectisome, a Complex Nanomachine for Protein Injection into Mammalian Cells. *EcoSal Plus* **8**, (2019).
8. Galán, J. E. & Wolf-Watz, H. Protein delivery into eukaryotic cells by type III secretion machines. *Nature* **444**, 567–573 (2006).
9. Type III Protein Secretion Systems in Bacterial Pathogens of Animals and Plants | Microbiology and Molecular Biology Reviews. https://journals.asm.org/doi/full/10.1128/MMBR.62.2.379-433.1998.
10. Hu, B., Lara-Tejero, M., Kong, Q., Galán, J. E. & Liu, J. In Situ Molecular Architecture of the Salmonella Type III Secretion Machine. *Cell* **168**, 1065-1074.e10 (2017).

11. Hu, B. *et al.* Visualization of the type III secretion sorting platform of Shigella flexneri. *Proc. Natl. Acad. Sci.* **112**, 1047–1052 (2015).
12. Kawamoto, A. *et al.* Common and distinct structural features of Salmonella injectisome and flagellar basal body. *Sci. Rep.* **3**, 3369 (2013).
13. Nans, A., Kudryashev, M., Saibil, H. R. & Hayward, R. D. Structure of a bacterial type III secretion system in contact with a host membrane in situ. *Nat. Commun.* **6**, 10114 (2015).
14. Butan, C., Lara-Tejero, M., Li, W., Liu, J. & Galán, J. E. High-resolution view of the type III secretion export apparatus in situ reveals membrane remodeling and a secretion pathway. *Proc. Natl. Acad. Sci.* **116**, 24786–24795 (2019).
15. Oikonomou, C. M. & Jensen, G. J. Electron cryo-tomography of bacterial secretion systems. *Microbiol. Spectr.* **7**, 10.1128/microbiolspec.PSIB-0019–2018 (2019).
16. Berger, C. *et al.* Structure of the Yersinia injectisome in intracellular host cell phagosomes revealed by cryo FIB electron tomography. *J. Struct. Biol.* **213**, 107701 (2021).
17. Diepold, A., Kudryashev, M., Delalez, N. J., Berry, R. M. & Armitage, J. P. Composition, Formation, and Regulation of the Cytosolic C-ring, a Dynamic Component of the Type III Secretion Injectisome. *PLOS Biol.* **13**, e1002039 (2015).
18. Diepold, A. *et al.* A dynamic and adaptive network of cytosolic interactions governs protein export by the T3SS injectisome. *Nat. Commun.* **8**, 1–12 (2017).
19. Rocha, J. M. *et al.* Single-molecule tracking in live Yersinia enterocolitica reveals distinct cytosolic complexes of injectisome subunits. *Integr. Biol.* **10**, 502–515 (2018).
20. Bernal, I. *et al.* Molecular Organization of Soluble Type III Secretion System Sorting Platform Complexes. *J. Mol. Biol.* **431**, 3787–3803 (2019).

21. Tachiyama, S. *et al.* Composition and Biophysical Properties of the Sorting Platform Pods in the Shigella Type III Secretion System. *Front. Cell. Infect. Microbiol.* **11**, 488 (2021).
22. Rocha, J., Corbitt, J., Yan, T., Richardson, C. & Gahlmann, A. Resolving Cytosolic Diffusive States in Bacteria by Single-Molecule Tracking. *Biophys. J.* **116**, 1970–1983 (2019).
23. Karslake, J. D. *et al.* SMAUG: Analyzing single-molecule tracks with nonparametric Bayesian statistics. *Methods* **193**, 16–26 (2021).
24. Elf, J. & Barkefors, I. Single-Molecule Kinetics in Living Cells. *Annu. Rev. Biochem.* **88**, 635–659 (2019).
25. Mullineaux, C. W., Nenninger, A., Ray, N. & Robinson, C. Diffusion of Green Fluorescent Protein in Three Cell Environments in Escherichia Coli. *J. Bacteriol.* **188**, 3442–3448 (2006).
26. Bellotto, N. *et al.* Dependence of diffusion in Escherichia coli cytoplasm on protein size, environmental conditions and cell growth. 2022.02.17.480843 (2022) doi:10.1101/2022.02.17.480843.
27. Minamino, T. & Macnab, R. M. FliH, a soluble component of the type III flagellar export apparatus of Salmonella, forms a complex with FliI and inhibits its ATPase activity. *Mol. Microbiol.* **37**, 1494–1503 (2000).
28. González-Pedrajo, B., Fraser, G. M., Minamino, T. & Macnab, R. M. Molecular dissection of Salmonella FliH, a regulator of the ATPase FliI and the type III flagellar protein export pathway. *Mol. Microbiol.* **45**, 967–982 (2002).
29. Blaylock, B., Riordan, K. E., Missiakas, D. M. & Schneewind, O. Characterization of the Yersinia enterocolitica Type III Secretion ATPase YscN and Its Regulator, YscL. *J. Bacteriol.* **188**, 3525–3534 (2006).

30. Bernal, I. *et al.* Structural analysis of ligand-bound states of the Salmonella type III secretion system ATPase InvC. *Protein Sci. Publ. Protein Soc.* **28**, 1888–1901 (2019).

31. Okabe, M., Minamino, T., Imada, K., Namba, K. & Kihara, M. Role of the N-terminal domain of FliI ATPase in bacterial flagellar protein export. *FEBS Lett.* **583**, 743–748 (2009).

32. Bai, F. *et al.* Assembly dynamics and the roles of FliI ATPase of the bacterial flagellar export apparatus. *Sci. Rep.* **4**, 6528 (2014).

33. Imada, K., Minamino, T., Uchida, Y., Kinoshita, M. & Namba, K. Insight into the flagella type III export revealed by the complex structure of the type III ATPase and its regulator. *Proc. Natl. Acad. Sci. U. S. A.* **113**, 3633–3638 (2016).

34. Case, H. B. & Dickenson, N. E. MxiN Differentially Regulates Monomeric and Oligomeric Species of the Shigella Type Three Secretion System ATPase Spa47. *Biochemistry* **57**, 2266–2277 (2018).

35. Diepold, A. *et al.* Deciphering the assembly of the Yersinia type III secretion injectisome. *EMBO J.* **29**, 1928–1940 (2010).

36. Muthuramalingam, M. *et al.* The Structures of SctK and SctD from Pseudomonas aeruginosa Reveal the Interface of the Type III Secretion System Basal Body and Sorting Platform. *J. Mol. Biol.* **432**, 166693 (2020).

37. Kinoshita, M., Namba, K. & Minamino, T. A positive charge region of Salmonella FliI is required for ATPase formation and efficient flagellar protein export. *Commun. Biol.* **4**, 1–14 (2021).

38. Chen, S. *et al.* Structural diversity of bacterial flagellar motors. *EMBO J.* **30**, 2972–2981 (2011).

39. McDowell, M. A. *et al.* Characterisation of Shigella Spa33 and Thermotoga FliM/N reveals a new model for C-ring assembly in T3SS. *Mol. Microbiol.* **99**, 749–766 (2016).

40. Wimmi, S. *et al.* Dynamic relocalization of cytosolic type III secretion system components prevents premature protein secretion at low external pH. *Nat. Commun.* **12**, 1625 (2021).

41. Lara-Tejero, M., Kato, J., Wagner, S., Liu, X. & Galán, J. E. A sorting platform determines the order of protein secretion in bacterial type III systems. *Science* **331**, 1188–1191 (2011).

42. Johnson, S. & Blocker, A. Characterization of soluble complexes of the Shigella flexneri type III secretion system ATPase. *FEMS Microbiol. Lett.* **286**, 274–278 (2008).

43. Zhang, Y., Lara-Tejero, M., Bewersdorf, J. & Galán, J. E. Visualization and characterization of individual type III protein secretion machines in live bacteria. *Proc. Natl. Acad. Sci.* **114**, 6098–6103 (2017).

44. Thomas, J., Stafford, G. P. & Hughes, C. Docking of cytosolic chaperone-substrate complexes at the membrane ATPase during flagellar type III protein export. *Proc. Natl. Acad. Sci.* **101**, 3945–3950 (2004).

45. Imada, K., Minamino, T., Kinoshita, M., Furukawa, Y. & Namba, K. Structural insight into the regulatory mechanisms of interactions of the flagellar type III chaperone FliT with its binding partners. *Proc. Natl. Acad. Sci.* **107**, 8812–8817 (2010).

46. Minamino, T., Kinoshita, M., Imada, K. & Namba, K. Interaction between FliI ATPase and a flagellar chaperone FliT during bacterial flagellar protein export. *Mol. Microbiol.* **83**, 168–178 (2012).

47. Kaniga, K., Delor, I. & Cornelis, G. R. A wide-host-range suicide vector for improving reverse genetics in Gram-negative bacteria: inactivation of the blaA gene of Yersinia enterocolitica. *Gene* **109**, 137–141 (1991).

48. Biteen, J. S. *et al.* Super-resolution imaging in live Caulobacter crescentus cells using photoswitchable EYFP. *Nat. Methods* **5**, 947–949 (2008).

49. Thompson, M. A., Lew, M. D., Badieirostami, M. & Moerner, W. E. Localizing and Tracking Single Nanoscale Emitters in Three Dimensions with High Spatiotemporal Resolution Using a Double-Helix Point Spread Function. *Nano Lett.* **10**, 211–218 (2010).

50. Pavani, S. R. P. *et al.* Three-dimensional, single-molecule fluorescence imaging beyond the diffraction limit by using a double-helix point spread function. *Proc. Natl. Acad. Sci.* **106**, 2995–2999 (2009).

51. Lew, M., Lew*, M. D., von Diezmann*, A. R. S. & Moerner, W. E. Easy-DHPSF open-source software for three-dimensional localization of single molecules with precision beyond the optical diffraction limit. *Protoc. Exch.* (2013) doi:10.1038/protex.2013.026.

52. Paintdakhi, A. *et al.* Oufti: an integrated software package for high-accuracy, high-throughput quantitative microscopy analysis. *Mol. Microbiol.* **99**, 767–777 (2016).